Hyperspectral imaging with laser-scanning sum-frequency generation microscopy

ADAM HANNINEN,[1] MING WAI SHU,[2] AND ERIC O. POTMA[2,3,*]

[1]*Department of Astronomy and Physics, University of California, Irvine, CA 92697, USA*
[2]*Department of Chemistry, University of California, Irvine, CA 92697, USA*
[3]*Beckman Laser Institute, Laser Microbeam and Medical Program, Irvine, CA 92617, USA*
[*]*epotma@uci.edu*

Abstract: Vibrationally sensitive sum-frequency generation (SFG) microscopy is a chemically selective imaging technique sensitive to non-centrosymmetric molecular arrangements in biological samples. The routine use of SFG microscopy has been hampered by the difficulty of integrating the required mid-infrared excitation light into a conventional, laser-scanning nonlinear optical (NLO) microscope. In this work, we describe minor modifications to a regular laser-scanning microscope to accommodate SFG microscopy as an imaging modality. We achieve vibrationally sensitive SFG imaging of biological samples with sub-μm resolution at image acquisition rates of 1 frame/s, almost two orders of magnitude faster than attained with previous point-scanning SFG microscopes. Using the fast scanning capability, we demonstrate hyperspectral SFG imaging in the CH-stretching vibrational range and point out its use in the study of molecular orientation and arrangement in biologically relevant samples. We also show multimodal imaging by combining SFG microscopy with second-harmonic generation (SHG) and coherent anti-Stokes Raman scattering (CARS) on the same imaging platform. This development underlines that SFG microscopy is a unique modality with a spatial resolution and image acquisition time comparable to that of other NLO imaging techniques, making point-scanning SFG microscopy a valuable member of the NLO imaging family.

References and links

1. B. R. Masters and P. T. C. So, *Handbook of Biomedical Nonlinear Optical Microscopy* (Oxford University Press, Oxford, 2008)
2. F. S. Pavone and P. J. Campagnola, *Second Harmonic Generation Imaging* (CRC Press, Boca Raton, 2013).
3. J. X. Cheng and X. S. Xie, *Coherent Raman Scattering Microscopy* (CRC Press, Boca Raton, 2013).
4. Y. R. Shen, "Surface properties probed by second-harmonic and sum-frequency generation," Nature **337**, 519–525 (1989).
5. C. Y. Chung, J. Boik, and E. O. Potma, "Biomolecular imaging with coherent nonlinear vibrational microscopy," Annu. Rev. Phys. Chem. **64**, 77–99 (2013).
6. H. F. Wang, L. Velarde, W. Gan, and L. Fu, "Quantitative sum-frequency generation vibrational spectroscopy of molecular surfaces and interfaces: lineshape, polarization, and orientation," Annu. Rev. Phys. Chem. **66**, 189–216 (2015).
7. M. Flörsheimer, C. Briller, and H. Fuchs, "Chemical imaging of interfaces by sum-frequency microscopy," Langmuir **15**, 5437–5439 (1999).
8. D. M. P. Hoffmann, K. Kuhnke, and K. Kern, "Sum-frequency generation microscope for opaque and reflecting samples," Rev. Sci. Instrum. **73**, 3221–3226 (2002).
9. K. Kuhnke, D. M. P. Hoffmann, X. C. Wu, A. M. Bittner, and K. Kern, "Chemical imaging of interfaces by sum-frequency generation microscopy: application to patterned self-assembled monolayers," Appl. Phys. Lett. **83**, 3830–3832 (2003).
10. K. Cimatu, and S. Baldelli, "Sum frequency generation microscopy of microcontact-printed mixed self-assembled monolayers," J. Phys. Chem. B **110**, 1807–1813 (2006).
11. K. A. Cimatu and S. Baldelli, "Chemical microscopy of surfaces by sum frequency generation imaging,"J. Phys. Chem. C **113**, 16575–16588 (2009).
12. K. A. Smith and J. C. Conboy, "A simplified sum-frequency vibrational imaging setup used for imaging lipid bilayer arrays," Anal. Chem. **84**, 8122–8126 (2012).

13. K. Locharoenrat, H. Sano, and Goro Mizutani, "Demonstration of confocal sum frequency microscopy," Phys. Status Solidi C **6**, 304-306 (2009).
14. H. C. Hieu, N. A. Tuan, H. Li, Y. Miyauchi, and G. Mizutani, "Sum frequency generation microscopy study of cellulose fibers," Appl. Spectrosc. **65**, 1254–1259 (2011).
15. H. Li, Y. Miyauchi, N. A. Tuan, G. Mizutani, and M. Koyano, "Optical sum frequency generation image of rice grains," J. Biomat. Nanobiotechnol. **3**, 286–291 (2012).
16. K. Inoue, M. Fujii, and M. Sakai, "Development of a non-scanning vibrational sum-frequency generation detected infrared super-resolution microscope and its application to biological cell," *Appl. Spectrosc.* **64**, 275–281 (2010).
17. S. Kogure, K. Inoue, T. Ohmori, M. Ishihara, M. Kikuchi, M. Fujii, and M. Sakai, "Infrared imaging of an A549 cultured cell by a vibrational sum-frequency generation detected infrared super-resolution microscope", Biomed. Opt. Express **13**, 13402–13406 (2010).
18. V. Raghunathan, Y. Han, O. Korth, N. H. Ge and E. O. Potma, "Rapid vibrational imaging with sum frequency generation microscopy," Opt. Lett. **36**, 3891–3893 (2011).
19. E. S. Lee, S. W. Lee, J. Hsu, and E. O. Potma, "Vibrationally resonant sum-frequency generation microscopy with a solid immersion lens," Biomed. Opt. Express **5**, 2125–2134 (2014).
20. Y. Han, V. Raghunathan, R. R. Feng, H. Maekawa, C. Y. Chung, Y. Feng, E. O. Potma, and N. H. Ge, "Mapping molecular orientation with phase sensitive vibrationally resonant sum-frequency generation microscopy," J. Phys. Chem. B **117**, 6149–6156 (2013).
21. Y. Han, J. Hsu, N. H. Ge and E. O. Potma, "Polarization-sensitive sum-frequency generation microscopy of collagen fibers," J. Phys. Chem. B **119**, 3356–3365 (2015).
22. C. M. Lee, K. Kafle, S. Huang, and S. H. Kim, "Multimodal broadband vibrational sum frequency generation (MM-BB-V-SFG) spectrometer and microscope," J. Phys. Chem. B **120**, 102–116 (2016).
23. H. Wang, T. Gao, and W. Xiong, "Self phase-stabilized heterodyne vibrational sum frequency generation microscopy," ACS Photonics **4**, 1839–1845 (2017).
24. T. Wilson and C. Sheppard, *Theory and Practice of Scanning Optical Microscopy* (Academic Press, London, 1984).
25. J. M. P. Nascimento and J. M. B. Dias, "Vertex component analysis: a fast algorithm to unmix hyperspectral data" IEEE Trans. Geosci. Remote Sens. **43**, 898–910 (2005).
26. M. Miljković, T. Chernenko, M. J. Romeo, B. Bird, C. Matthäus, and M. Diem, "Label-free imaging of human cells: algorithms for image reconstruction of Raman hyperspectral datasets," Analyst **135**, 2002–2013 (2010).
27. J. T. Tabarangao and A. D. Slepkov, "Mimicking multimodal contrast with vertex component analysis of hyperspectral CARS images," J. Spectrosc. **2015**, 575807 (2015).
28. S. Psilodimitrakopoulos, S. I. C. O. Santos, I. Amat-Roldan, A. K. N. Thayil, D. Artigas, and P. Loza-Alvarez, "In vivo, pixel-resolution mapping of thick filaments orientation in nonfibrilar muscle using polarization-sensitive second harmonic generation microscopy," J. Biomed. Opt. **14**, 014001 (2009).
29. P. J. Su, W. L. Chen, Y. F. Chen, and C. F. Dong, "Determination of collagen nanostructure from second-order susceptibility tensor analysis," Biophys. J. **100**, 2053–2062 (2011).
30. A. E. Tuer, S. Krouglov, N. Prent, R. Cisek, D. Sandkuijl, K. Yasufuku, B. C. Wilson, and V. Barzda, "Nonlinear optical properties of type I collagen fibers studied by polarization dependent second harmonic generation microscopy," J. Phys. Chem. B **115**, 12759–12769 (2011).
31. I. Rocha-Mendoza, D. R. Yankelevich, M. Wang, K. M. Reiser, C. W. Frank, and A. Knoesen, "Sum frequency vibrational spectroscopy: the molecular origins of the optical second-order nonlinearity of collagen," Biophys. J. **93** 4433–4444 (2007).
32. R. M. J. Brown, A. C. Millard, and P. J. Campagnola, "Macromolecular structure of cellulose studied by second-harmonic generation imaging microscopy," Opt. Lett. **28**, 2207–2209 (2003).
33. Y. Marubashi, T. Higashi, S. Hirakawa, S. Tani, T. Erata, M. Takai, and J. Kawamata, "Second harmonic generation measurements for biomacromolecules: celluloses," Opt. Rev. **11**, 385–387 (2004).
34. M. Zimmerley, R. Younger, T. Valenton, D. C. Oertel, J. L. Ward, and E. O. Potma, "Molecular orientation in dry and hydrated cellulose fibers: a coherent anti-Stokes Raman scattering microscopy study," J. Phys. Chem. B **114**, 10200–10208 (2010).
35. C. M. Lee, N. M. A. Mohamed, H. D. Watts, J. D. Kubicki, and S. H. Kim, "Sum-frequency-generation vibration spectroscopy and density functional theory calculations with dispersion corrections (DFT-D2) for cellulose Iα and Iβ," J. Phys. Chem. B **117**, 6681–6692 (2013).
36. C. M. Lee, K. Kafle, Y. B. Park, and S. H. Kim, "Probing crystal structure and mesoscale assembly of cellulose microfibrils in plant cell walls, tunicate tests, and bacterial films using vibrational sum frequency generation (SFG) spectroscopy," Phys. Chem. Chem. Phys. **16**, 10844–10853 (2014).
37. L. Zhang, Z. Lu, L. Velarde, L. Fu, Y. Pu, S. Y. Ding, A. J. Ragauskas, H. F. Wang, and B. Yang, "Vibrational spectral signatures of crystalline cellulose using high resolution broadband sum frequency generation vibrational spectroscopy (HR-BB-SFG-VS)," Cellulose **22**, 1469–1484 (2015).
38. D. Zheng, L. Lu, Y. Li, K. F. Kelly, and S. Baldelli, "Compressive broad-band hyperspectral sum frequency generation microscopy to study functionalized surfaces," J. Phys. Chem. Lett. **7**, 1781–1787 (2016).
39. P. J. N. Kett, M. T. L. Casford, and P. B. Davies, "Sum frequency generation vibrational spectroscopy of cholesterol in hybrid bilayer membranes," J. Phys. Chem. B **117**, 6455–6465 (2013).
40. L. Fu, S. L. Chen, and H. F. Wang, "Validation of spectra and phase in sub-cm^{-1} resolution sum-frequency gen-

eration vibrational spectroscopy through internal heterodyne phase-resolved measurement," J. Phys. Chem. B **120**, 1579–1589 (2016).

41. C. Y. Lin, J. L. Suhalim, C. Nien, M. D. Miljkovic, M. Diem, J. Jester, and E. O. Potma, "Picosecond spectral coherent anti-Stokes Raman scattering (CARS) imaging with principal component analysis of meibomian gland", J. Biomed. Opt. **16**, 021104 (2011).

42. S. Bégin, B. Burgoyne, V. Mercier, A. Villeneuve, R. Vallée, and D. Côté, "Coherent anti-Stokes Raman scattering hyperspectral tissue imaging with a wavelength-swept system," Biomed. Opt. Express **2**, 1296–1306 (2011).

43. E. T. Garbacik, J. L. Herek, C. Otto, and H. L. Offerhaus, "Rapid identification of heterogeneous mixture components with hyperspectral coherent anti-Stokes Raman scattering imaging," J. Raman Spectrosc. **43**, 651–655 (2012).

44. J. L. Suhalim, C. Y. Chung, M. B. Lilledahl, R. S. Lim, M. Levi, B. J. Tromberg, and E. O. Potma, "Characterization of cholesterol crystals in atherosclerotic plaques using stimulated Raman scattering and second-harmonic generation microscopy," Biophys. J. **102**, 1988–1995 (2012).

45. Y. Ozeki, W. Umemura, Y. Otsuka, S. Satoh, H. Hashimoto, K. Sumimura, N. Nishizawa, K. Fukui, and K. Itoh, "High-speed molecular spectral imaging of tissue with stimulated Raman scattering," Nat. Photon. **6**, 845–851 (2012).

46. D. Zhang, P. Wang, M. N. Slipchenko, D. Ben-Amotz, A. M. Weiner, and J. X. Cheng, "Quantitative vibrational imaging by hyperspectral stimulated Raman scattering microscopy and multivariate curve resolution analysis," Anal. Chem. **85**, 98–106 (2013).

47. X. Y. Dow, E. L. DeWalt, J. A. Newman, C. M. Dettmar, and G. J. Simpson, "Unified theory for polarization analysis in second harmonic and sum frequency microscopy," Biophys. J. **111**, 1553–1568 (2016).

48. C. Hirose, N. Akamatsu, and K. Domen, "Formulas for the analysis of surface sum-frequency generation spectrum by CH stretching modes of methyl and methylene groups," J. Chem. Phys. **96**, 997–1004 (1992).

49. C. Hirose, H. Yamamoto, N. Akamatsu, and K. Domen, "Orientation analysis by simulation of vibrational sum frequency generation spectrum: CH stretching bands of the methyl group," J. Phys. Chem. **97**, 10064–10069 (1993).

50. K. Reiser, P. Stoller, and A. Knoesen, "Three-dimensional geometry of collagenous tissues by second harmonic polarimetry," Sci. Rep. **7**, 2642 (2017).

1. Introduction

In nonlinear optical (NLO) microscopy, two or more photons combine to interact with the sample and induce a nonlinear polarization, which produces radiation that can be captured with a far-field photodetector. Over the past two decades or so, various NLO imaging techniques have been developed and some of them are now regularly used to support biological and biomedical research [1]. A subset of these NLO techniques are based on the coherent driving of molecules in the focal volume, thus producing coherent radiation. Examples include second- and third-harmonic generation (SHG, THG) [2], coherent anti-Stokes Raman scattering (CARS) and stimulated Raman scattering (SRS) [3]. All these techniques exhibit an intrinsic three-dimensional resolution, and can be conveniently carried out with laser-scanning microscopes, which feature rapid imaging capabilities and are easy to use for routine imaging applications. In fact, a typical laser-scanning NLO microscope incorporates several detectors for capturing various nonlinear optical signals simultaneously, enabling multimodal imaging.

Vibrationally resonant sum-frequency generation (SFG) is another member of the family of coherent NLO techniques. In SFG, the sample is illuminated by a mid-IR beam at ω_1 and a vis/NIR beam at ω_2, producing a signal at $\omega_3 = \omega_1 + \omega_2$ [4–6]. It can be considered a hybrid between SHG and CARS. Like SHG, SFG is a second-order optical effect, which relies on non-centrosymmetries in the sample. Like CARS, SFG is based on a vibrational excitation, followed by an anti-Stokes Raman interaction. However, unlike CARS, the vibrational excitation is driven by a low energy, mid-infrared photon (ω_1), rather than by a two-photon Raman interaction. When the energy of the mid-IR photon is near a vibrational resonance, the SFG response is enhanced, giving the technique its vibrational sensitivity. Because of these properties, SFG microscopy is sensitive to the same structures as seen in nonresonant SHG microscopy, with the important difference that it adds (vibrational) spectroscopic contrast to the images.

Despite these attractive properties, SFG microscopy is not frequently used for biological imaging applications. A fundamental complication for the SFG modality is that the mid-IR beam driving the resonant vibration is incompatible with standard microscope optics that accommodate the visible/NIR spectrum. For this reason, SFG microscopes often follow very different

excitation and detection strategies compared to a laser-scanning microscope. In particular, several wide-field, non-collinear illumination schemes have been developed and implemented for spectroscopic and microscopic SFG applications. In such wide-field configurations, the SFG radiation from a large area is commonly captured by an objective lens and projected onto a CCD camera [7–12]. Although useful for spectroscopic studies of surfaces, such microscope designs are less attractive for rapid imaging of three-dimensional cell and tissue samples. An alternative non-collinear excitation scheme, which has been proven more successful for imaging bulk second-order optical nonlinearities in biological samples, uses oblique illumination of the mid-IR beam (ω_1) whereas the ω_2 beam is tightly focused by a high numerical aperture (NA) lens [13–15]. In the latter system a confocal detector is used, making it possible to acquire SFG images with sub-μm resolution. Despite these advantages, such a non-collinear design is not compatible with other forms of NLO imaging, thus complicating convenient integration of SFG into a multimodal microscope.

Laser-scanning microscopes make use of collinear illumination of the excitation beams, suggesting that an integrated SFG modality should be based on a collinear excitation geometry as well. Sakai and co-workers implemented a collinear illumination by using a regular lens to focus the ω_1 and ω_2 beams to a common, though shallow, focus [16, 17]. In the case of thin samples, the phase-matched signal in this configuration propagates in the forward direction, along with the excitation beams. If detection is performed with a high NA microscope objective, SFG images can be acquired with a resolution defined by the collecting lens. Even better performance is obtained if the illuminating lens is replaced by a high NA objective, consistent with the layout of a standard laser-scanning microscope. Because the mid-IR wavelengths are not supported by commercial refractive microscope objectives, a reflective objective can be used, which are inherently achromatic. Such a microscope focuses both beams to a tight focal spot, enabling SFG imaging with sub-μm resolution, while retaining much of the design elements of common NLO microscopes. This approach has enabled detailed SFG imaging studies of biological structures with non-vanishing second-order nonlinearities, such as collagen [18–21] and cellulose [22] fibers.

So far, collinear SFG microscopes have used sample scanning to generate images [18, 22, 23], which is inherently slow. In this work, we demonstrate laser-scanning SFG microscopy by integrating the SFG modality directly into a conventional NLO microscope with only minor modifications. The resulting imaging platform is capable of generating SFG images at unprecedented rates, similar to the frame rate of the accompanying SHG and CARS signals acquired on the same system. We demonstrate the utility of the laser-scanning SFG microscope by performing hyperspectral and polarization-resolved imaging studies of various relevant biological structures, highlighting the unique information attainable with SFG microscopy beyond what can be obtained with existing modalities. The advances and imaging examples showed herein underline that SFG imaging is an attractive and feasible addition to the multimodal NLO microscope, providing new spectroscopic contrast previously inaccessible in routine imaging applications.

2. Methods

2.1. Light source

The layout of the laser-scanning SFG microscope is shown in Fig. 1. The main light source is a picosecond Er$^+$-doped fiber laser (aeroPULSE, NKT Photonics) centered at 1030 nm (6 ps pulse width, 76 MHz repetition rate) that drives a synchronously-pumped optical parametric oscillator (OPO). The OPO, which is optimized for NIR and MIR generation (Levante IR OPO, APE Berlin), includes a fanned periodically-poled nonlinear crystal, generating a spectrally tunable signal in the 1350 nm to 2000 nm range that is resonant in the OPO cavity. The idler beam, which is generated upon each passage of the signal pulse through the crystal, is coupled out of the cavity and used as the ω_1 beam in the SFG experiments. The idler can be tuned from

2200 nm to 4300 nm corresponding to molecular vibrations in the 2320 cm^{-1} to 4550 cm^{-1} range. In addition to the signal (NIR) and idler (MIR) delivered by the OPO, the residual pump beam can also be used in the NLO experiments. For SFG, we use the idler beam for the ω_1 excitation, whereas the 1030 nm beam is used for the ω_2 excitation. CARS is achieved by using the 1030 nm beam for the pump interaction and the OPO signal for the Stokes interaction. The 1030 nm beam is also used for generating SHG signals. The beams are conditioned with spatial filters and their linear polarization state is controlled with a polarizer and a half-wave plate. For the mid-infrared beam, a low-order magnesium fluoride half-waveplate ($3\lambda/2$ retardance at 2860 cm^{-1}) and a BaF$_2$ holographic wire grid polarizer (extinction ratio 150:1 at 3300 cm^{-1}) are used. For the near-infrared beam, an achromatic half-waveplate and a calcite Glan-Taylor polarizer are utilized. Using two custom dichroic mirrors (Layertec GmbH), the beams are combined in a collinear fashion, as shown schematically in Fig. 1.
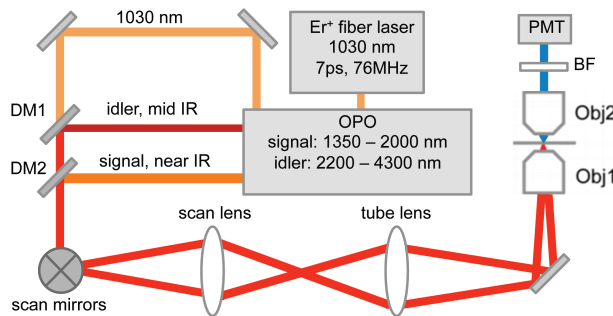

Fig. 1. Schematic of the SFG microscope. Galvanometric mirrors are part of an Olympus Fluoview 300 laser scanner, and excitation and collection optics are part of an Olympus IX71 frame. PMT: photomultiplier, BF: bandpass filter, Obj: microscope objective, DM: dichroic mirror.

2.2. Microscope

The microscope system consists of a modified laser-scanning module (Fluoview 300, Olympus) and inverted microscope frame (IX71, Olympus). To accommodate the NIR and MIR beams, the scan lens ($f = 50$ mm) and tube lens ($f = 180$ mm) are replaced by CaF$_2$ lenses, which are transparent to the relevant range of frequencies used in the experiments. The beams are steered into the laser-scanning module, passing a set of Al-coated galvanometric mirrors, and coupled into the microscope where they are focused by a 0.65NA, 74x, Cassegrain reflective objective (5007, Beck). The NLO signals are captured in the forward direction by a refractive condenser lens (achromatic/aplanatic condenser, max. NA = 1.40, Olympus) and passed through a short pass and a bandpass filter before being detected by a photomultiplier tube (PMT). In our study, we focus on the vibrational modes near 2945 cm^{-1}, resulting in a SFG and CARS signal near 790 nm. The SHG signal is detected at 515 nm. The average illumination power of the MIR and NIR beams onto the sample were in the 1–4mW and 15–40mW range, respectively. The lateral resolution of the SFG images is dictated by the reflective objective and amounts to $\sim 0.6\ \mu$m [18]. The axial resolution is inherently affected by the central obfuscation of the Cassegrain objective [19, 24] and is approximately 15 μm.

Note that the polarization conditions in collinear SFG microscopy are markedly different from those in surface SFG spectroscopy experiments. The latter implies that different combinations of tensor elements of the nonlinear susceptibility are probed. The tensor elements are written as $\chi_{ijk}^{(2)}$, where (i, j, k) are the polarization directions of the $(\omega_3, \omega_2, \omega_1)$ fields in

the molecular frame. In all SFG experiments reported herein, the linear polarization direction of the ω_1 and ω_2 beams are identical, resulting in excitation fields in the focal plane that have their strongest component polarized in the lateral (XY) plane. No analyzer is used in front of the detector, implying that the experiments are most sensitive to the $\chi^{(2)}_{iXX}$ and $\chi^{(2)}_{iYY}$ tensor elements, where $i = X, Y$ and (XY) are the coordinates of the laboratory frame [21].

2.3. Single photon counting

We have incorporated a single photon counter scheme, which provides higher sensitivity than the more conventional analog detection for the signal levels relevant to our experiments. The current output from the red/NIR sensitive PMT (7422-50, Hamamatsu) is preamplified (TIA60, Thorlabs) and sent to a discriminator (F-100T, Advanced Research Instruments, CO). The discriminator outputs a digital TTL pulse of 5V and a duration of 5ns every time a photon is detected. The advantages here are palpable, as it increases the signal to noise ratio by eliminating the contributions below the discriminator's threshold. A possible drawback is the lower dynamic range of digital detection, as a maximum of one photon per pulse can be detected. However, practical counting rates for the SFG signal are well below the pulse repetition rate (76 MHz), which constitutes a favorable regime for single photon counting. The TTL output pulses are conditioned with a function waveform generator (AFG3102, Tektronix) to yield pulses with an amplitude of 6V and a duration of 10ns. The latter parameters optimizes the integration of the signal pulses by the Fluoview acquisition card.

2.4. Sample

A rat tail, dissected from a rat, was stored at -20 ^{o}C until use. Individual tendon fascicles about 100 μm long were removed from the tendon bundles under a dissecting microscope, and flattened between two cover slips before SFG imaging. The cholesterol sample was obtained by dissolving cholesterol powder (C75209, Sigma-Aldrich) in chloroform and allowing the solute to recrystallize on the cover slip upon evaporation of the solvent. The medium-sized powdered cellulose fibers (c6288, Sigma-Aldrich) were suspended in a few drops of water, then air dried onto a cover slip.

2.5. Image analysis

Hyperspectral images of the samples were acquired to reconstruct the spectra in the CH stretching range (2800 cm^{-1} to 3100 cm^{-1}). Image acquisition times were typically 1 s/frame (512 x 512 pixels). For hyperspectral SFG imaging, images were taken for different wavelength settings of the ilder beam, using manual adjustment of the OPO in between images. Hyperspectral datasets consisted of 20 spectral acquisitions. To facilitate visual inspection of the data, some of the hyperspectral datasets were analyzed with vertex component analysis (VCA) using home-written code in MATLAB. VCA is an algorithm for spectral unmixing, providing pseudocolor contrast highlighting regions within the field of view with distinct spectral features [25]. Spectral analysis with VCA has been used previously for Raman [26] and coherent Raman microscopy [27].

3. Results

3.1. *Hyperspectral SFG reveals molecular orientation in fibrous structures*

Like SHG microscopy, SFG microscopy is sensitive to molecular orientation. To acquire orientation information in SHG imaging, the polarization direction of the incident fields is typically varied. In SFG microscopy, however, orientation of molecules can be obtained directly from variations in the spectral features, information that is inaccessible in SHG measurements. In Fig. 2, a tendon tissue is visualized with both SFG and SHG contrast. The SHG results are shown in panels (a)–(c). In Fig. 2(a), the polarization orientation of the incident beam is aligned with the long axis of the collagen fiber bundles, resulting in a strong signal. When the incident polarization is rotated by 90°, as shown in Fig. 2(b), the signal is significantly lower, except for the region where the fibers are bent. The polar plot in Fig. 2(c), acquired from the boxed region of interest, shows a clear dependence of the SHG signal on the polarization direction of the incident beam, which can be related to the orientation of the collagen fibers [28–30]. Similar information can be obtained from SFG images. In Fig. 2(d), the SFG at 2945 cm^{-1} is shown when the polarization direction of both beams are aligned with the main axis of the fibers, while panel 2(e) shows the SFG image when the input polarization is rotated by 90°. Although the features in the image appear sharper in the SFG channel due to a much higher anisotropy of the resonant signal [21], overall the SFG and SHG images appear very similar.
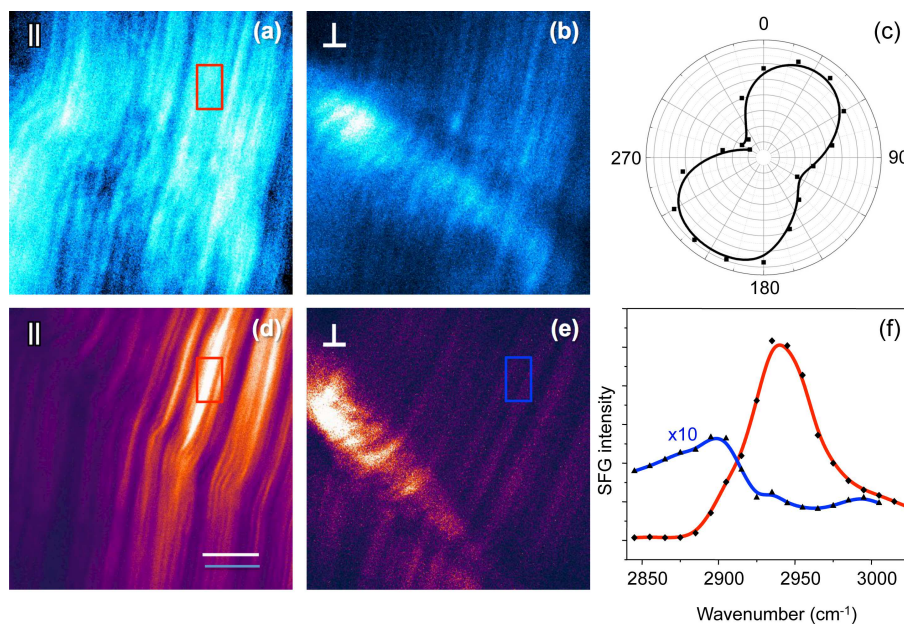

Fig. 2. SHG and SFG imaging of rat tail tendon, a collagen I rich tissue. a) SHG image obtained with the polarization orientation of the incident beam parallel to the long axis of the collagen fibers. b) SHG image similar to a), but with the polarization orientation rotated by 90°. c) SHG polarization plot taken in the red region of interest shown in a). Direction refers to the polarization orientation of the incident beam. d) SFG image at 2945 cm^{-1} of the same sample and with the polarization orientation of both beams aligned with the main axis of the collagen tissue. e) SFG image similar to e), but with the polarization orientation rotated by 90°. f) SFG spectra extracted from the hyperspectral data stack. Red spectrum refers to the region of interest in d) and blue spectrum refers to the region of interest indicated in e). Scale bar is 15 μm.

The differences between SHG and SFG imaging become clearer when the SFG image is spectrally resolved. In panel 2(f), two SFG spectra are extracted from the boxed areas of panels 2(d) and 2(e), which are part of a hyperspectral data stack recorded between 2840 cm^{-1} and 3050 cm^{-1}. The red spectrum is obtained from the area indicated in panel 2(d), when the polarization direction of the beams is aligned with the long axis of the fibers. This spectrum shows a clear resonance that peaks at 2945 cm^{-1} and mimics previously published SFG spectra in this range [21, 31]. The blue spectrum is acquired in the same area, but with the polarization of the incident beams rotated by 90°. In the latter setting, SFG signal is significantly weaker. The 2945 cm^{-1} peak is almost completely suppressed for this polarization setting. However, the blue spectrum shows a clear and reproducible feature around 2890 cm^{-1} [21]. This feature is strongest when the polarization of the ω_1 beam is orthogonal to the long fiber axis.
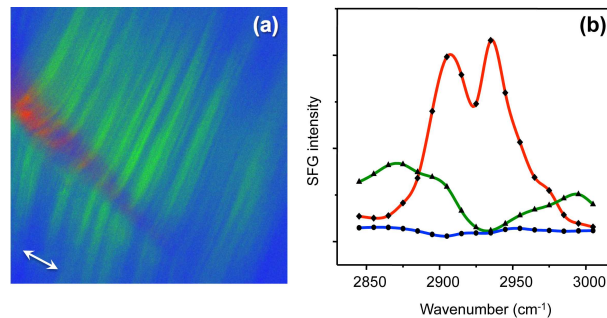

Fig. 3. Multivariate analysis of collagen rich tissue. a) Vertex component analysis (VCA) image showing three end-members in red, green and blue, based on a hyperspectral SFG data stack. The arrow indicates the polarization direction of the incident beams. b) Corresponding end-member SFG spectra extracted from the VCA.

These different spectral features allow a direct reading of the collagen orientation without the need to change the polarization. This is shown in Fig. 3, which shows the VCA image of three end-members extracted from the SFG hyperspectral data stack associated with Fig. 2(e). Note that the three end-member spectra retrieved by the VCA are found by linear unmixing of the hyperspectral dataset, and constitute spectral profiles (red, green, blue) through which each pixel can be properly represented as an RGB color. The spectrally unmixed image thus allows for an easy inspection of spectrally significant differences in the dataset. Although the unmixing does not necessarily separate the response into individual vibrational modes or tensor elements, the retrieved spectra carry meaningful information on collagen's SFG spectral response. The green spectrum, depicted in Fig. 3(b), is reminiscent of the collagen spectrum when the ω_1 polarization direction is orthogonal to that of the fiber alignment. This endmember spectrum shows similarities with the blue spectrum in Fig. 2(f). The region where the fibers are bent yields a very different spectrum, represented by the red spectrum in Fig. 3(b). This spectrum appears to be a combination of modes, including the 2945 cm^{-1} mode, that are driven in the red region under these polarization conditions. The aligned and bent fibers are clearly demarcated by their SFG spectra, which reflects their orientation, without changing the polarization of the incident beams. Note that a similar feat is not possible with SHG imaging, where rotation of the polarization is required to obtain information on molecular orientation.

Another example of hyperspectral SFG imaging of fibrous structures is shown in Fig. 4. Figure 4(a) shows an SFG image of a cellulose fiber. Similar to collagen I fibers, cellulose fibers of the Iβ allomorph exhibit a non-vanishing second-order optical nonlinearity [32–34]. A strong resonant SFG signal from the cellulose fiber is observed when the ω_1 beam is tuned near 2940 cm^{-1} [14, 35–37]. The corresponding SHG signal is shown in panel 4(b). The VCA image
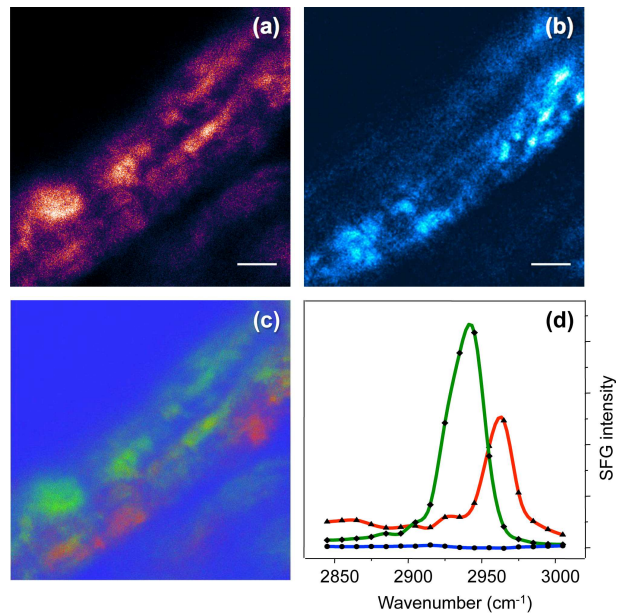
Fig. 4. Hyperspectral SFG imaging of a cellulose fiber. a) SFG image taken at 2945 cm^{-1}. b) Corresponding SHG image. c) VCA image of the SFG hyperspectral data stack, showing three end-members in red, green and blue. d) SFG end-member spectra obtained from the VCA. Scale bar is 10 μm.

from the SFG hyperspectral recording is shown in panel 4(c). The VCA spectral segmentation identifies two dominant spectral components, shown in Fig. 4(d), that correspond to different regions in the fiber. The SFG spectrum of cellulose Iβ is dependent on molecular orientation and packing [22, 36], and thus the VCA image highlights microdomains in the fiber with different arrangements of the cellulose units. Similar to the collagen example above, the molecular arrangement information is encoded in the spectral domain and is acquired with a single setting of the incident polarization.

3.2. Hyperspectral SFG imaging of crystalline structures

Besides visualizing fibrous structures, the SFG microscope is sensitive to molecular micro-crystals that exhibit non-centrosymmetry. An example is given in Fig. 5, which shows SFG imaging results on micro-crystals of cholesterol. At 2850 cm^{-1}, the symmetric methylene stretching vibration, a strong SFG signal is observed from cholesterol. This is evident in Fig. 5(a), where several bright domains can be discerned along with dimmer crystalline structures. The signal from these structures is strongly dependent on the polarization direction of the incident beams, as is evident from the SHG polar plot shown in Fig. 5(b), which shows the (non-resonant) second-order optical signal for two selected regions in Fig. 5(a). The SFG spectra from the same regions of interest are shown in Fig. 5(c), featuring several modes in the CH-stretching range. The mode amplitudes of the retrieved spectrum, however, differ from previous SFG measurements of cholesterol in monolayers [39, 40]. The latter can be attributed to the different excitation (polarization) geometry used in SFG microscopy and the fact that the molecular ordering in crystalline cholesterol is different from its arrangement in monolayers. The amplitude of the different modes depends strongly on the orientation of the micro-crystals. This property is utilized in Fig. 5(d), where images taken at the 2955 cm^{-1} (blue), 2925 cm^{-1}

(green), and 2845 cm^{-1} (red) vibrational energies are normalized and overlaid in a color map. The resulting image illustrates the different orientation of the crystal domains as encoded in the SFG spectra.
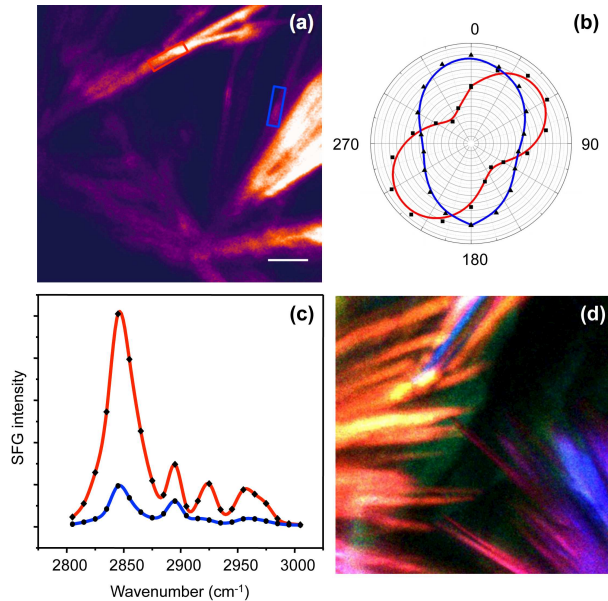

Fig. 5. SFG imaging of cholesterol microcrystals. a) SFG image at 2845 cm^{-1}. Scale bar is 10 μm. b) SHG polar plots obtained in the red and blue boxed regions of interest of the image in a). c) SFG spectra extracted from the regions of interest in image a). The red spectrum is obtained from the red box, whereas the blue spectrum is obtained from the blue box. d) Composite SFG image formed by overlaying images taken at 2955 cm^{-1} (blue), 2925 cm^{-1} (green), and 2845 cm^{-1} (red).

3.3. Multimodal SFG imaging

In previous subsections we have shown SFG and SHG images recorded from the same field of view. It is also possible to acquire CARS images with the same laser-scanning microscope. To generate a CARS image, we add the signal beam of the OPO (ω_s), which acts as the Stokes interaction in the CARS process while the ω_2 ($\lambda = 1030$ nm) beam acts as the pump interaction. For instance, if we are interested in driving a vibrational resonance at 2845 cm^{-1}, the Stokes beam is tuned to 1457 nm. Note that both the signal and idler beams are delivered by the OPO, and are thus related as $\omega_s = \omega_2 - \omega_1$. In the case all three beams are present (ω_1, ω_2 and ω_s), the CARS and SFG processes both take place. By tuning the idler to a given frequency, both the CARS and the SFG processes drive the sample at the same vibrational energy, because $\omega_2 - \omega_s = \omega_1$. However, since $2\omega_2 - \omega_s = \omega_1 + \omega_2 = \omega_3$, the frequencies of the CARS and the SFG signals are identical as well. Hence, whereas the SHG and SFG signals can be measured simultaneously in different channels, the CARS signal emerges in the same wavelength channel as the SFG signal. To obtain both CARS and SFG images of a given sample, images can be recorded consecutively. SFG is measured when blocking the ω_s beam, and CARS is detected when blocking the ω_1 beam. An example is shown in Fig. 6, displaying the SFG and CARS image of a cluster of cholesterol microcrystals visualized at a vibrational energy of 2845 cm^{-1}. Although both modalities probe methylene stretching modes of cholesterol in the images shown,

the SFG image is sensitive only to spatial symmetries captured by $\chi^{(2)}$, while the CARS image results from the bulk allowed $\chi^{(3)}$ of the material. The sensitivity to molecular orientation is different between the modalities, resulting in different features in the image. The availability of both the $\chi^{(2)}$ and $\chi^{(3)}$ response at the same vibrational energy is helpful for a more complete analysis of molecular arrangements at the microscale. For example, the combination of SFG and Raman spectral profiles can facilitate the band assignments in the CH-stretching range of microcrystallites like the cholesterol sample shown here. SFG band assignments in this vibrational range can be challenging [6], and the additional information on the polarization properties of spectral signatures provided by Raman can help determine mode symmetry and orientation.
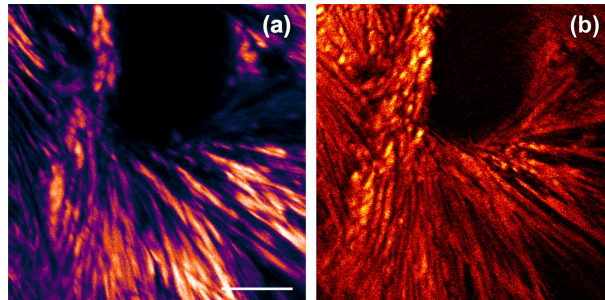

Fig. 6. Cholesterol microcrystals visualized with a) SFG and b) CARS. Vibrational driving frequency in both images is set at 2845 cm^{-1}. Scale bar is 10 μm.

4. Discussion

In this work, we have integrated vibrationally sensitive SFG as a modality into a laser-scanning, nonlinear optical microscope. This advance enabled us to acquire bright SFG images from biological samples with an image acquisition rate of 1 frame/s, similar to the acquisition rate of other NLO modalities. Such a frame rate is almost two orders of magnitude higher than previously reported point-scanning SFG microscopes. With this improvement in scanning speed and ease-of-use, the SFG modality is no longer an exotic variant of NLO microscopy, but can be considered a practical addition to the multimodal NLO microscope.

It is useful to compare the signal strength of SFG microscopy to existing imaging techniques. For instance, at vibrational resonance, the SFG signal is typically stronger than the SHG signal measured from the same sample. In our system, the SHG signal is generated at 515 nm by 15–40 mW of the 1030 nm beam. The SFG signal is generated at the same average power of the 1030 nm beam (ω_2), by adding 1–4 mW of the mid-IR beam (ω_1). Under these conditions, the SFG signal of collagen-rich tissue at 2945 cm^{-1} is almost 10 times as strong as the accompanying SHG signal. When tuned off-resonance, the SFG signal is comparable to the nonresonant SHG signal. This example shows that the vibrationally resonant SFG signal can be very strong and thus constitutes a practical imaging modality. In terms of signal strength, the image acquisition speed can be improved even more. Currently, the frame rate is limited by the scanning hardware/software of our microscope rather than by the magnitude of the SFG signal.

One of the reasons why SFG has become a feasible contrast option is the practicality of generating the mid-IR pulsed radiation needed for the SFG technique. In most SFG spectroscopic studies, an amplified femtosecond laser system is the standard light source for producing the ω_1 and ω_2 beams. However, amplified laser systems are less suitable for rapid imaging studies, because the pulse repetition rate is typically too low for fast image acquisition. A high repetition rate oscillator in combination with a synchronously pumped OPO is a much more attractive option for laser-scanning microscopy. Such light sources are commonly used in coherent Raman

scattering (CRS) microscopy studies and are commercially available. The OPO used here is optimized for generating an idler beam in the mid-IR range, but otherwise the light source is identical to a "conventional" light source for picosecond CRS microscopy.

The NIR/MIR system used in this study enabled us to perform SFG, SHG and CARS imaging studies, using exclusively excitation beams with wavelengths longer than 1 μm. This wavelength regime is interesting for imaging tissue samples with a thickness of up to a few hundred μm. For thicker tissues, the use of MIR light is not practical, as absorption by tissue water gives rise to unwanted heating. The studies discussed in this work were limited to samples of ~100 μm thickness, in which case no noticeable heating effects were observed.

The faster acquisition and integration into a standard microscope platform has enabled us to carry out hyperspectral SFG imaging studies. Hyperspectral SFG microscopy is not new, as several broadband implementations have been described in the literature, both for non-collinear [11, 38] and collinear [22] SFG microscopes. Here we introduce narrowband hyperspectral SFG microscopy as an attractive option for spectral mapping of three-dimensional biological samples. This approach is very similar to picosecond hyperspectral CARS [41–43] and SRS [44–46] microscopy, where the wavelength of one of the incident beams is systematically varied in between images. At 1 frame/s, the acquisition time of a hyperspectral datastack is limited by the time it takes to change the wavelength. Currently, the wavelength is tuned manually by adjusting the position of the fan-poled nonlinear crystal in the OPO. Automation of this procedure is straightforward, and would enable the acquisition of a hyperspectral datastack within one minute or so.

Through several examples, we have shown that hyperspectral SFG imaging is sensitive to molecular orientation. The use of multivariate analysis of the datastacks has yielded intuitive, spectrally-unmixed images that highlight differences in molecular orientation within the field of view. Although a deeper analysis of the orientation of molecular vibrational modes in the laboratory frame is beyond the scope of this work, it is possible to extract detailed information from the images shown. Recent work has discussed several formalisms of connecting the information from the molecular frame to experimentally accessible parameters [47]. In combination with the proper spectral assignments of the observed bands in the CH-stretching range [48, 49], future work will focus on translating hyperspectral datasets into information on the effective orientation of the molecular modes within the probing volume.

The hyperspectral SFG imaging examples discussed in this work emphasize the use of the technique for studying molecular orientation in detail. However, the utility of spectral SFG mapping is not limited to molecular orientation studies. For instance, examination of image features with new and unexpected SFG spectral features can lead to the discovery of new markers of molecular properties that are difficult or impossible to extract from nonresonant SHG images. The blue spectrum shown in Fig. 2(f), for instance, contains a weak but reproducible spectral feature at 2890 cm^{-1}. This feature is maximized when the polarization of the incident beams is orthogonal to the long axis of the fibers, i.e. this signature can be considered a marker for the short axis of the fiber. This also implies that the 2890 cm^{-1} can be used to visualize collagen fibers that are aligned longitudinally along the axial dimension. In SHG microscopy, longitudinally oriented fibers are very challenging to visualize [50], making it difficult to generate pictures of three-dimensional fiber distributions. The use of SFG, which uses unique information encoded in the spectral dimension, might offer a solution for directly and confidently imaging of out-of-plane fibers.

Although the current multimodal NLO microscope allows the generation of hyperspectral SFG images with good contrast, several improvements would enhance the image quality even more. First, the singlet CaF$_2$ scan and tube lenses used in this study suffer from chromatic aberrations. Because the spectral gap between the NIR and MIR beams is substantial, chromatic aberrations are inevitable. These aberrations are expected to deteriorate the image quality for

large scan angles and thus limit the workable field of view of the microscope. The design of refractive lenses that are achromatic over the NIR/MIR range would improve the field of view and image quality accordingly. Second, although the reflective objective used in our SFG studies is achromatic, the Cassegrain reflector blocks the center portion of the beam and limits the angular components needed for forming a focal volume that is highly confined in three-dimensions [19]. As a consequence, compared to refractive objectives, the use of the reflective objective elongates the focal volume along the optical axis and decreases the axial resolution. The design and incorporation of a fully refractive objective lens with achromaticity over the desired NIR/MIR range, would significantly benefit the SFG modality.

5. Conclusion

In this work, we have made simple modifications to a commercial laser-scanning microscope to enable the generation of SFG images in an easy and rapid manner. The improvement in image acquisition time by almost two orders of magnitude compared to previous point-scanning SFG microscopes has also allowed us to record hyperspectral SFG datastacks and perform multivariate analysis of various spectral signatures of the sample. These imaging capabilities make it possible to study the microscopic arrangement of molecules in detail. The advances discussed in this work add some of the unique properties of SFG spectroscopy to the convenience of a laser-scanning microscope, establishing SFG imaging as a valuable member of the family of NLO microscopy techniques.

Disclosures

The authors declare that there are no conflicts of interest related to this article.